Received: Added at production | Revised: Added at production | Accepted: Added at production
DOI: xxx/xxxx

ARTICLE TYPE

Implicit large eddy simulation of passive scalar transfer in compressible planar jet

Youming Tai | Tomoaki Watanabe | Koji Nagata

[1]Department of Aerospace Engineering, Nagoya University, Nagoya, Japan

Correspondence
*Tomoaki Watanabe. Email: watanabe.tomoaki@c.nagoya-u.jp

Summary

Implicit large eddy simulation (ILES) of passive scalar transfer in compressible turbulence is evaluated for subsonic and supersonic turbulent planar jets. The ILES used in this study relies on fully-explicit numerical schemes for spatial and temporal discretization and low-pass and shock-capturing filters used as an implicit subgrid-scale (SGS) model. The ILES results are compared with the DNS database of the same flows. The ILES results exhibit good agreements with the DNS for 1st and 2nd order statistics of velocity and passive scalar. The scalar transport by turbulent velocity fluctuations is well captured by the ILES. The temporal evolution of the jet strongly depends on the jet Mach number, where a higher Mach number results in the delay of jet development. The Mach number dependence of velocity and passive scalar fields is consistent between the ILES and DNS. The low-pass filters used as the implicit SGS model contribute to the dissipation of turbulent kinetic energy and scalar variance. Under the present numerical conditions, the filters account for about 50% of the dissipation in a fully-developed turbulent jet. The dissipation rate in the ILES, which is the sum of the grid-scale and SGS dissipation rates, is very close to the dissipation rate in the DNS, and the amount of the SGS dissipation is well controlled by the low-pass filters. The filters also dump numerical oscillations in the velocity field caused by strong pressure waves outside the supersonic jet at the high Mach number.

KEYWORDS:
Implicit large eddy simulation, Turbulent mixing, Supersonic jet

1 | INTRODUCTION

The mixing of diffusive scalars in compressible turbulence plays an important role in industrial reactive flows since the turbulent mixing process often governs the progress of chemical reactions. Numerical simulations have been widely used for predicting

---

[0]This version (accepted manuscript) is free to view and download for private research and study only. The final version is available on https://doi.org/10.1002/fld.4924.

Abbreviations: ILES, implicit large eddy simulation; DNS, direct numerical simulation compressible flows in realistic problems. In comparison with experimental approaches, numerical simulations can significantly improve efficiency and safety in developing engineering products such as internal combustion engines because experiments with engine models usually take a long time and might emit harmful gas [1]. In aerospace engineering, the promotion of turbulent mixing in supersonic flows is an important issue for designing propulsion systems [2].

Large eddy simulation (LES) [3] solves low-pass filtered governing equations, which provide temporal evolution of a large-scale flow field resolved on a coarse computational grid. The filtered governing equations contain terms described by small-scale fluctuations, which are not resolved on the coarse grid. Therefore, the LES relies on models for the terms arising from unresolved small-scale (subgrid-scale, SGS) fluctuations, and accuracy of the LES depends on the SGS models. Conventional LES employs explicit SGS models, by which the SGS terms are calculated with grid-scale quantities. One of the examples of the explicit model is the Smagorinsky model [3]. If scalar transfer is also simulated by the LES, an eddy diffusivity model is often combined with the Smagorinsky model to close the low-pass filtered scalar transport equation. The LES with the explicit SGS models has been validated for various flows such as a fully expanded jet [4] and a round jet issuing into a cross flow [5]. However, it is also known that the Smagorinsky model can lead to unphysical effects on a simulated flow field. For instance, the effective Reynolds number of the flow is artificially reduced by the eddy viscosity model [6, 7], and numerical instabilities may arise from incorrect predictions of dissipative effects by the model [8].

An alternative approach is based on implicit models for the SGS terms. It has been known that nonlinear truncation errors of explicit filtering schemes can also provide implicit SGS closures even when no explicit SGS model is added at all. Following this concept, high-order low-pass filters are often used as the implicit SGS models, where the filters contribute to the dissipation of turbulent fluctuations. LES with the implicit SGS models is called implicit LES (ILES) [9]. Unlike the explicit models, the numerical low-pass filters in the ILES can reasonably minimize large-scale energy dissipation introduced by the model. Moreover, numerical schemes of the ILES are fairly simple when explicit filters are applied as the implicit SGS models. Interests in the ILES have grown substantially in recent years, and the ILES has been tested in various turbulent flows [7, 10, 11, 12, 13, 14, 15, 16].

When a flow with passive scalar transfer is simulated in the LES, the SGS model is also required for the filtered scalar transport equation. The low-pass filter can also be used as the implicit SGS model for the scalar field. In this case, the filter must account for the dissipation of scalar fluctuations in the SGS. The ILES of turbulent flows with passive scalar transfer has been tested for incompressible flows, e.g., a channel flow [17], grid turbulence [18], and a planar jet [19]. The ILES was also tested for stratified turbulence (active scalar), whose statistical properties were well predicted by the ILES [20]. Numerical simulations of reacting flows often combine the LES with simulations based on computational particles such as a filtered density function method [21] or a particle-based solver of scalar transport equations [22, 23]. These particle-based simulations often use a model for molecular diffusion, which is called a mixing model. Some mixing models used in the particle-based simulations are improved by using a model parameter calculated with a single, inert passive scalar simulated in the LES [24]. Thus, the accurate LES of passive scalar may contribute to better predictions of turbulent reacting flows. Most previous studies on the ILES of turbulent mixing consider incompressible flows [17, 18, 19], and the ILES has hardly been verified for the passive scalar transfer in high-speed, compressible flows.

In this study, we attempt to evaluate the ILES of compressible turbulence with passive scalar transfer. The ILES conducted in this paper relies on fully explicit schemes for spatial and temporal discretization and low-pass and shock-capturing filters used as the implicit SGS model, all of which are easy to implement in in-house numerical codes. The ILES is tested by simulating a temporally evolving planar jet whose initial velocity is set in a subsonic or supersonic level, for which the DNS database is available from our previous study [25]. The rest of this paper is organized as follows. The numerical methods of the present ILES are provided in Section 2. Section 3 describes the planar jet simulated in this study as well as computational parameters. The ILES results are discussed in comparison with the DNS in Section 4. Finally, conclusion is presented in Section 5.

2 | IMPLICIT LARGE EDDY SIMULATION OF COMPRESSIBLE TURBULENCE WITH PASSIVE SCALAR TRANSFER

2.1 | Governing equations

We consider a compressible flow with an assumption of ideal gas, whose evolution is described by the compressible Navier-Stokes equations. We also consider passive scalar transfer, which is described by an advection-diffusion equation. Once the equations are normalized with appropriate reference quantities, the governing equations are written by

$$\frac{\partial \rho}{\partial t} + \frac{\partial \rho u_j}{\partial x_j} = 0, \tag{1}$$

$$\frac{\partial \rho u_i}{\partial t} + \frac{\partial \rho u_i u_j}{\partial x_j} = -\frac{\partial P}{\partial x_i} + \frac{1}{Re}\frac{\partial \tau_{ij}}{\partial x_j}, \tag{2}$$

$$\frac{\partial \rho T}{\partial t} + \frac{\partial \rho T u_j}{\partial x_j} = -(\gamma - 1)P\frac{\partial u_j}{\partial x_j} + \frac{\gamma}{RePr}\frac{\partial}{\partial x_j}\left(\mu \frac{\partial T}{\partial x_j}\right) + \frac{\gamma - 1}{Re}\tau_{ij}\frac{\partial u_i}{\partial x_j}, \tag{3}$$

$$\frac{\partial \rho \varphi}{\partial t} + \frac{\partial \rho \varphi u_j}{\partial x_j} = \frac{1}{ScRe}\frac{\partial}{\partial x_j}\left(\mu \frac{\partial \varphi}{\partial x_j}\right), \tag{4}$$

$$P = \rho T. \tag{5}$$

Here, t is the time, x_i is the position, ρ is the density, u_i is the i-th component of the velocity vector, T is the temperature, P is the pressure, μ is the viscosity coefficient, and $\gamma = c_p/c_v$ is the specific heat ratio. The viscous stress tensor τ_{ij} is assumed to be

$$\tau_{ij} = \mu\left(\frac{\partial u_i}{\partial x_j} + \frac{\partial u_j}{\partial x_i} - \frac{2}{3}\delta_{ij}\frac{\partial u_k}{\partial x_k}\right). \tag{6}$$

Nondimensional variables f can be related to their dimensional counterparts $\hat{f}$ as

$$x_i = \frac{\hat{x}_i}{l_r};\;\; u_i = \frac{\hat{u}_i}{u_r};\;\; \rho = \frac{\hat{\rho}}{\rho_r};\;\; t = \frac{\hat{t}u_r}{l_r};\;\; P = \frac{\hat{P}}{\rho_r u_r^2};\;\; T = \frac{\hat{T}R}{u_r^2};\;\; \varphi = \frac{\hat{\varphi}}{\varphi_r};\;\; \mu = \frac{\hat{\mu}}{\mu_r}. \tag{7}$$

Here, $R = c_p - c_v$ is the gas constant and the subscript r refers to the reference quantity: l_r, u_r, ρ_r, ϕ_r, and μ_r are, respectively, the reference values of length, velocity, density, scalar, and viscosity coefficient. Nondimensional parameters in Eqs. (2-4) are defined as

$$Re = \frac{\rho_r u_r l_r}{\mu_r};\;\; Pr = \frac{\mu c_p}{k};\;\; Sc = \frac{\mu}{\rho_r D}. \tag{8}$$

2.2 | Numerical methods of ILES

The ILES code used in this study is based on fully explicit numerical schemes for temporal and spatial discretization, a high-order low pass filter, and a shock-capturing filter. Message Passing Interface (MPI) functions are utilized for parallel computation. In the ILES code, the governing equations are solved on a relatively coarse grid with the low-pass filter and the shock-capturing filter dissipating the energy of fluctuations since the ILES does not resolve small scales of turbulent fluctuations, where the dissipation mostly takes place. These filters work as an implicit SGS model of the LES. As no explicit SGS models are used in the ILES, the main difference between ILES and DNS codes is in the additional filters. Therefore, the ILES code used in this study is developed by adding the filtering schemes to a DNS code based on finite difference schemes. This DNS code was used in our previous studies on compressible turbulent boundary layers and planar jets [25, 26, 27]. The present ILES relies on two filtering schemes: a group of conventional low-pass filters and a shock-capturing filter. Here, the strength of the shock-capturing filter is adjusted to prevent Gibbs oscillations around discontinuities. These filters are applied to ρ, ρu_i, ρT, and $\rho\varphi$ after the temporal integration at each time step. Time integration of Euler terms including advection and pressure terms is performed with an explicit five-step fourth-order Runge-Kutta scheme [28], whereas the remaining terms arising from viscous effects, molecular diffusion, and thermal conduction are temporally integrated by an explicit first-order Euler scheme. Spatial derivatives are calculated by an 8th-order central difference scheme except for regions near computational boundaries, where the derivatives are calculated with lower-order central difference schemes and non-centered difference schemes to strengthen local stability without extra loss of accuracy. Details of the spatial and temporal discretization schemes can be found in Wang et al. [29].

Different filtering schemes are used as the low-pass filter depending on the distance from the computational boundaries. A central selective filter [30] is used in an interior region far away from the boundaries and regions close to periodic boundaries. Hereafter, a variable f defined at an orthogonal grid point (i, j, k) is denoted by $f_{i,j,k}$, where $i = 1, ..., N_x$, $j = 1, ..., N_y$, and $k = 1, ..., N_z$ represent locations of a grid point in x, y, and z directions, respectively. The selective filter in the x direction, F_x,

TABLE 1 Coefficients of the selective filter using 11-point stencils ($d_{-j} = d_j$).

d_0	0.215044884112
d_1	−0.187772883589
d_2	0.123755948787
d_3	−0.059227575576
d_4	0.018721609157
d_5	−0.002999540835

applied to a variable $f_{i,j,k}$ is expressed as

$$F_x * f_{i,j,k} = f_{i,j,k} - \sum_{n=-5}^{5} d_n f_{i+n,j,k}, \tag{9}$$

where the coefficients $d_j = d_{-j}$ are provided in Table 1. When point i is close to the computational boundaries facing in the x direction, point $i+n$ can be located outside the computational domain unless periodic boundary conditions are applied. Therefore, the non-centered low-pass filters in [31] are applied for the regions near non-periodic boundaries instead of the central selective filter. These non-centered filters applied for $i = 1, ..., 5$ are expressed as

$$\begin{aligned}
F_x * f_{1,j,k} &= f_{1,j,k} - 2^{-10}\left(f_{1,j,k} - 5f_{2,j,k} + 10f_{3,j,k} - 10f_{4,j,k} + 5f_{5,j,k} - f_{6,j,k}\right),\\
F_x * f_{2,j,k} &= f_{2,j,k} - 2^{-10}\left(-5f_{1,j,k} + 26f_{2,j,k} - 55f_{3,j,k} + 60f_{4,j,k} - 35f_{5,j,k} + 10f_{6,j,k} - f_{7,j,k}\right),\\
F_x * f_{3,j,k} &= f_{3,j,k} - 2^{-10}\left(10f_{1,j,k} - 55f_{2,j,k} + 126f_{3,j,k} - 155f_{4,j,k} + 110f_{5,j,k} - 45f_{6,j,k} + 10f_{7,j,k} - f_{8,j,k}\right),\\
F_x * f_{4,j,k} &= f_{4,j,k} - 2^{-10}\big(-10f_{1,j,k} + 60f_{2,j,k} - 155f_{3,j,k} + 226f_{4,j,k}\\
&\qquad - 205f_{5,j,k} + 120f_{6,j,k} - 45f_{7,j,k} + 10f_{8,j,k} - f_{9,j,k}\big),\\
F_x * f_{5,j,k} &= f_{5,j,k} - 2^{-10}\big(5f_{1,j,k} - 35f_{2,j,k} + 110f_{3,j,k} - 205f_{4,j,k} + 251f_{5,j,k}\\
&\qquad - 210f_{6,j,k} + 120f_{7,j,k} - 45f_{8,j,k} + 10f_{9,j,k} - f_{10,j,k}\big).
\end{aligned}$$

The filters applied at the points near the boundary of $i = N_x - 4, ..., N_x$ can be defined in the same way as these filters. The filters are repeatedly applied to the variables in three directions as $F_x * [F_y * (F_z * f)]$.

The shock-capturing filter proposed in [32] is used for avoiding numerical instabilities due to Gibbs oscillations. The shock-capturing filter in the x direction, $F_x^{(S)}$, is calculated as

$$\begin{aligned}
F_x^{(S)} * f_{i,j,k} = f_{i,j,k} - \Big[&-0.5\left(\sigma^{(x)}_{i-1,j,k} + \sigma^{(x)}_{i,j,k}\right)\left(-d_1^{(S)} f_{i-2,j,k} + d_2^{(S)} f_{i-1,j,k} - d_2^{(S)} f_{i,j,k} + d_1^{(S)} f_{i+1,j,k}\right)\\
&+ 0.5\left(\sigma^{(x)}_{i,j,k} + \sigma^{(x)}_{i+1,j,k}\right)\left(-d_1^{(S)} f_{i-1,j,k} + d_2^{(S)} f_{i,j,k} - d_2^{(S)} f_{i+1,j,k} + d_1^{(S)} f_{i+2,j,k}\right)\Big],
\end{aligned} \tag{10}$$

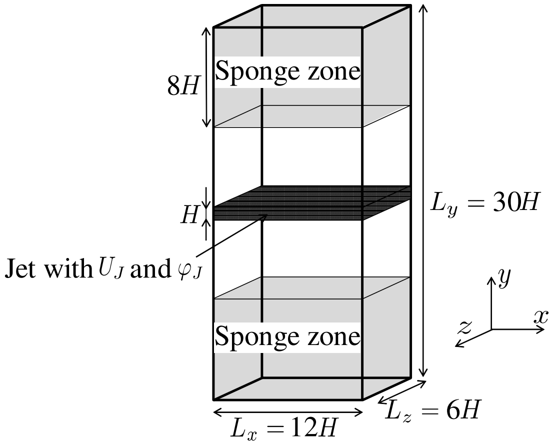

FIGURE 1 Numerical simulation of a temporally-evolving compressible planar jet.

with $d_1^{(S)} = 0.039617$ and $d_2^{(S)} = 0.210383$, where the filter strength $\sigma^{(x)}$ is given by

$$\sigma^{(x)} = \frac{1}{2}\left(1 - \frac{r_m}{r^{(x)}} + \left|1 - \frac{r_m}{r^{(x)}}\right|\right). \tag{11}$$

Here, r_m is a threshold parameter of the filter, and the shock sensor index $r^{(x)}$ is a measure of the strength of shock waves used for the filter in the x direction. The shock wave strength can be quantified with dilatation $\Theta = \partial u_j / \partial x_j$. Therefore, $r^{(x)}$ is dynamically determined by the high-wavenumber component of the dilatation D and the local sound speed $c = \sqrt{\gamma P/\rho}$ at each grid point [32]:

$$r_{i,j,k}^{(x)} = \frac{0.5\left[(D_{i,j,k} - D_{i+1,j,k})^2 + (D_{i,j,k} - D_{i-1,j,k})^2\right]}{c_{i,j,k}^2/(\Delta_x)_{i,j,k}^2} + 10^{-16}, \tag{12}$$

$$D_{i,j,k} = \frac{1}{4}\left(-\Theta_{i-1,j,k} + 2\Theta_{i,j,k} - \Theta_{i+1,j,k}\right), \tag{13}$$

where Δ_x is the grid spacing in the x direction. With this definition of $\sigma^{(x)}$, the shock-capturing filter effectively acts only in the regions with strong dilatation at high wavenumbers. Similarly to the low-pass filters presented above, the shock-capturing filter is also applied to ρ, ρu_i, ρT, and $\rho\varphi$ in three directions as $F_x^{(S)} * [F_y^{(S)} * (F_z^{(S)} * f)]$. The constant threshold parameter r_m plays an important role in discriminating between turbulent fluctuations and Gibbs oscillations arising from the shock waves. In this study, ILES is performed with $r_m = 1$, which is determined from r_m-dependence of the ILES in Section 4.1.

3 | TEST PROBLEM

3.1 | Passive scalar transfer in compressible planar jet

The ILES of passive scalar transfer in compressible turbulence is tested by simulating a temporally-evolving compressible planar jet of air shown in Figure 1. The flow is the same as in our previous DNS [25]. The temporal problem is considered in this study because the computational cost is lower than its spatial counterpart. This means that a higher Reynolds number in the DNS can be achieved for a temporal jet than a spatial jet with the same computational resource. x, y, and z denote the streamwise, lateral, and spanwise directions, respectively. The velocity components in these directions are denoted as u_x, u_y, and u_z. The temporal jet develops with time in the computational domain, where periodic boundary conditions are applied in the x and z directions. Because the flow is homogeneous in the x and z directions, spatial averages for statistical analysis are taken on x-z planes as functions of time and y. This average is denoted by $\langle * \rangle$.

The ILES assumes the gas constant $R = 287$ [J/(kg·k)] and the specific heat ratio $\gamma = 1.4$. The dimensional viscosity coefficient $\hat{\mu}$ is given as a function of temperature by Sutherland's law:

$$\hat{\mu} = \left(\frac{\hat{T}}{T_a}\right)^{3/2} \frac{T_a + S}{\hat{T} + S}, \tag{14}$$

with $T_a = 273$ [K] and $S = 110.4$ [K]. The initial mean streamwise velocity and width of the jet are U_J and H, respectively. The jet is assumed to carry a passive scalar φ, whose initial values are equal to φ_J in the jet and 0 in the ambient fluid. The temporal planar jet is initialized with a velocity profile comprising the mean streamwise velocity $\langle u_x \rangle$ and fluctuating velocity components u_i' $(i = x, y, z)$. A hyperbolic-tangent profile is adopted to specify the initial mean streamwise velocity as $\langle \hat{u}_x \rangle = 0.5U_J + 0.5U_J \tanh[(H - 2|\hat{y}|)/\theta_S]$, where $\theta_S = 0.03H$ is the shear layer thickness. The initial velocity fluctuations are generated by an artificial-turbulence generator that converts random numbers into spatially-correlated fluctuations with a diffusion process [33]. Similarly, the initial profile of φ is given by $\varphi = 0.5\varphi_J + 0.5\varphi_J \tanh[(H - 2|\hat{y}|)/\theta_S]$. The initial pressure is uniform and is set to atmospheric pressure 1.013×10^5 [Pa]. The initial temperature of the ambient fluid is $T_0 = 300$ [K]. The initial temperature profile for $|\hat{y}| \leq 0.5H$ is given by the Crocco-Busemann relation written as a function of $\langle \hat{u}_x \rangle$ [34]:

$$\hat{T}(y) = T_0 \left\{ 1 + 0.5\,(\gamma - 1) \frac{\langle \hat{u}_x \rangle}{U_J} \left(1 - \frac{\langle \hat{u}_x \rangle}{U_J} \right) M_{\mathrm{J}}^2 \right\}. \tag{15}$$

With this relation, the initial temperature in the jet is $T_0 = 300$ [K]. Then, the initial density profile is calculated with the equation of state for ideal gas. The Prandtl number is $Pr = 0.7$ and the Schmidt number is $Sc = 1$. The jet Mach number M_J and Reynolds number Re_J are defined as

$$M_J = \frac{U_J}{\sqrt{\gamma R T_0}}, \quad Re_J = \frac{\rho_0 U_J H}{\mu_J}, \tag{16}$$

where μ_J is the viscosity coefficient at 300 [K]. The ILES is performed for $(Re_J, M_J) = (14000, 0.6)$ and $(Re_J, M_J) = (14000, 2.6)$, for which the DNS database is available from our previous paper [25]. Strong effects of compressibility appear at $M_J = 2.6$. Once M_J and Re_J are specified, Eq. (16) gives dimensional values of U_J and H. The reference quantities are chosen as $l_r = H$, $u_r = U_J$, $\rho_r = \rho_0$, $\varphi_r = \varphi_J$, and $\mu_r = \mu_J$.

3.2 | Computational conditions

The ILES uses a three-dimensional rectangular computational box with the size of $(L_x, L_y, L_z) = (12H, 30H, 6H)$ as shown in Figure 1. The computational boundaries in the x and z directions are treated with periodic boundary conditions. Subsonic outflow boundary conditions of Navier-Stokes characteristic boundary conditions [28] are applied to the boundaries in the y direction. Furthermore, the regions of $|y| > 7H$ are treated as sponge zones, where the second-order low-pass filter [35] is applied to suppress pressure waves toward the boundaries. The interior region between the two sponge zones is large enough for the jet development. Structured grids are used to discretize the computational domain, where the number of grid points in each direction is $(N_x, N_y, N_z) = (480, 300, 240)$. The ILES is also conducted with a smaller number of grid points, $(N_x, N_y, N_z) = (360, 300, 180)$. Here, $N_y = 300$ is used in both grid settings because the simulations with much smaller N_y do not resolve well the initial shear layers at the edges of the jet. The ILES with the coarse grid setting is used for assessing grid dependence and most results presented in this paper are taken from the ILES with the fine grid. The grid points are uniformly spaced in the x and z directions while the grid size in the y direction increases towards the boundaries in the y direction. Here, the grid location in the y direction is determined by a mapping function presented in [25]. The DNS used for comparisons with the ILES was performed with $(N_x, N_y, N_z) = (2200, 1400, 1100)$ [27]. Nondimensional time increment in each time step is chosen as the minimum value of Δt in the computational domain, where Δt is calculated as

$$\Delta t = \mathrm{CFL} \times \left[(u_i/\Delta_i) + M_J^{-1} (\Delta_i \Delta_i)^{-1/2} \right]^{-1}, \tag{17}$$

with CFL = 0.9. Here, summation is taken for the repeated index i and Δ_i is the nondimensional grid size in the i direction. The threshold parameter r_m of the shock-capturing scheme is set to 1, for which the shock-capturing filter acts only for the early time of the simulations because the jet velocity decays with time. This value of r_m is chosen after the ILES is performed for a wide range of r_m as shown in Section 4.1.

For improving statistical convergence, the ILES is repeated 70 times by changing initial velocity fluctuations, and the results of all simulations are used as statistical samples. Spatial averages $\langle\ \rangle$ are taken on x-z planes as functions of y and time by using all samples of 70 simulations. Fluctuations of f from the average are denoted by $f' = f - \langle f \rangle$, and root-mean-squared (rms) fluctuations of f can be calculated as $f_{rms} = \langle f'^2 \rangle^{1/2} = \sqrt{\langle f^2 \rangle - \langle f \rangle^2}$.

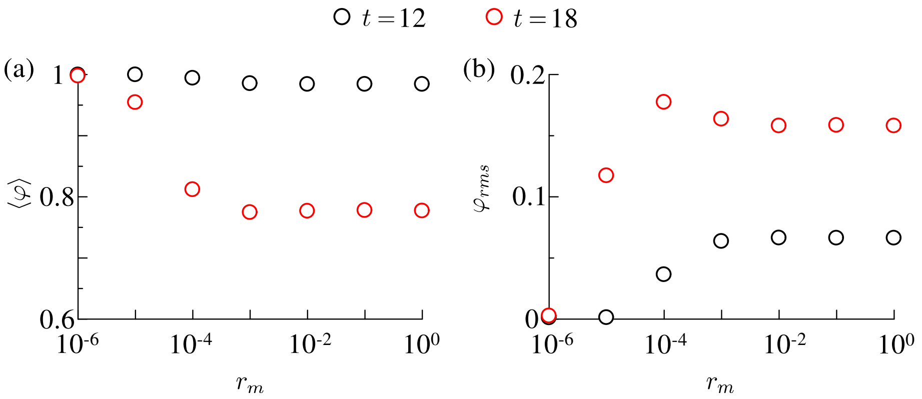

FIGURE 2 r_m dependence of (a) mean scalar $\langle\varphi\rangle$ and (b) rms scalar fluctuations φ_{rms} at the center of the jet with $M_\mathrm{J} = 2.6$. The results are taken at $t = 12$ and 18.

4 | RESULTS AND DISCUSSIONS

4.1 | Threshold of the shock-capturing filter

The threshold of the shock-capturing filter, r_m, is determined based on the threshold dependence of ILES. The ILES is performed for r_m between 10^{-6} and 10^0. We also confirmed that the simulations with $r_m \geq 10^1$ stop due to numerical instability for $M_J = 2.6$. Figure 2 shows mean scalar $\langle\varphi\rangle$ and rms scalar fluctuations φ_{rms} as functions of r_m. The results are taken at the center of the jet with $M_\mathrm{J} = 2.6$ for two time steps of $t = 12$ and 18. As r_m increases, $\langle\varphi\rangle$ tends to decrease and φ_{rms} increases. At $t = 18$, $\langle\varphi\rangle$ is expected to be smaller than the initial value in the jet ($\langle\varphi\rangle = 1$) because of mixing in the turbulent jet. Smaller r_m results in stronger artificial dissipation of velocity fluctuations in the ILES. This artificial dissipation can suppress the turbulent transition of the jet if r_m is too small. Therefore, $\langle\varphi\rangle$ at $t = 18$ approaches 1 as r_m is decreased. Similarly, the shock-capturing filter with small r_m causes an unphysical decay of φ_{rms}, which becomes small as r_m is decreased. When r_m is taken between 10^{-3} and 10^0, $\langle\varphi\rangle$ and φ_{rms} hardly depend on r_m. In this range of r_m, the shock-capturing filter hardly causes the delay of the turbulent transition and the artificial decay of turbulence while it prevents the numerical instability due to shock waves. Therefore, we present the results of the ILES with $r_m = 1$ in the rest of the paper. It should be noted that the filter with $r_m = 1$ does not cause any problems associated with the artificial dissipation in the ILES for $M_\mathrm{J} = 0.6$.

4.2 | Temporal development of turbulent jet

Figures 3 and 4 show instantaneous streamwise velocity u_x and scalar φ on a x-y plane at five time instances. Turbulence begins to appear near the edges of the jet, where the shear instability produces turbulence. As time advances, small-scale fluctuations arise in the entire jet region, and the jet spreads in the y direction. Initial turbulent transition of the shear layers is delayed for higher M_J: the small-scale fluctuations due to the shear layers can be seen at $t = 6$ for $M_J = 0.6$ and $t = 12$ for $M_J = 2.6$.

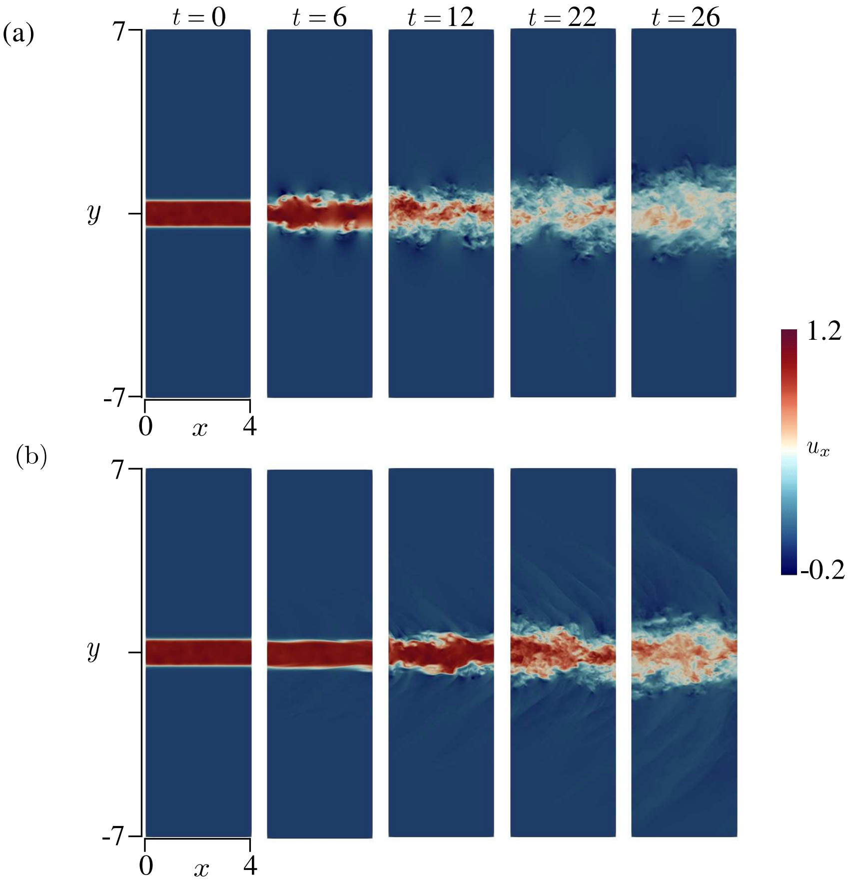

FIGURE 3 Instantaneous streamwise velocity on a x-y plane for (a) $M_J = 0.6$ and (b) 2.6 at $t = 0, 6, 12, 22$, and 26 (from left to right). A whole computational domain is not shown in this figure.

Figure 4(a) indicates that large-scale vortices at the edges of the jet cause engulfment of the ambient flow into the jet region for $M_J = 0.6$ at $t = 6$. However, the engulfment is not clearly found for $M_J = 2.6$ at $t = 12$. Similar suppression of the engulfment due to high Mach number effects was also observed in previous experimental studies of mixing layers [36, 37]. As mixing of φ between the jet and ambient flow proceeds with time, the jet tends to have φ lower than 1. Values of φ in Figure 4 indicates that scalar mixing is faster for the lower Mach number. For $M_J = 2.6$, pressure waves radiated from the jet appear as sharp velocity jumps outside the jet in Figure 3(b). They propagate diagonally from the initial shear layers around $t = 12$. Discontinuities arising from the strong pressure waves are treated well with the shock-capturing filter in the ILES without having numerical instabilities.

Figure 5 presents temporal evolutions of the jet half-width based on mean streamwise velocity (b_u) and mean passive scalar (b_φ). Here, we define the half-width as the distance from $y = 0$ to the location where the mean velocity or scalar reaches half of the value at $y = 0$. For early time, b_u^2 and b_φ^2 are constant as expected for the potential core region of the jet. A self-similarity analysis predicts $b_u^2 \sim t$ and $b_\varphi^2 \sim t$. Indeed, b_u^2 and b_φ^2 tend to linearly increase in proportion to t for late time. b_u is smaller

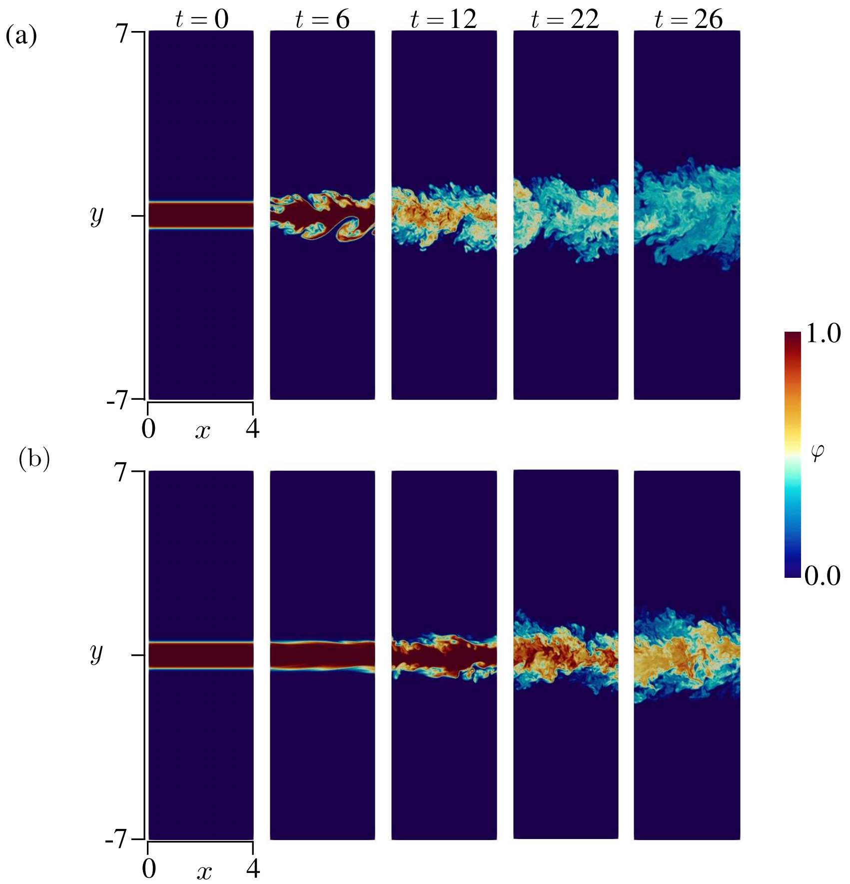

FIGURE 4 Instantaneous passive scalar φ on a x-y plane for (a) $M_J = 0.6$ and (b) 2.6 at $t = 0, 6, 12, 22$, and 26 (from left to right). A whole computational domain is not shown in this figure.

than b_φ as also observed in previous experiments of turbulent jets [38, 39], indicating that the scalar is more diffused than the streamwise momentum.

Figure 6 displays the lateral profiles of mean streamwise velocity $\langle u_x \rangle$ and mean scalar $\langle \varphi \rangle$ at $t = 6$ and 26 divided by their centerline values denoted with the subscript c. Here, the lateral coordinate y is also normalized by b_u or b_φ. The mean profiles at $t = 6$ for $M_J = 0.6$ are already close to those at $t = 26$, However, the jet with $M_J = 2.6$ has top-hat profiles of the mean velocity and scalar at $t = 6$ because of the slower jet development for higher M_J. However, in the later time at $t = 26$, the mean streamwise velocity and scalar profiles from the ILES collapse onto a single curve for both Mach numbers. In Figures 5 and 6, the ILES agrees well with the DNS [25], and the mean flow evolution is well predicted by the ILES conducted in this study.

4.3 | Statistical properties of the fully-developed turbulent jet

Figure 7 shows the lateral profiles of rms values of streamwise velocity fluctuations $(u_x)_{rms}$, lateral velocity fluctuations $(u_y)_{rms}$, spanwise velocity fluctuations $(u_z)_{rms}$, and passive scalar fluctuations φ_{rms} in the ILES and DNS. Here, the rms values are

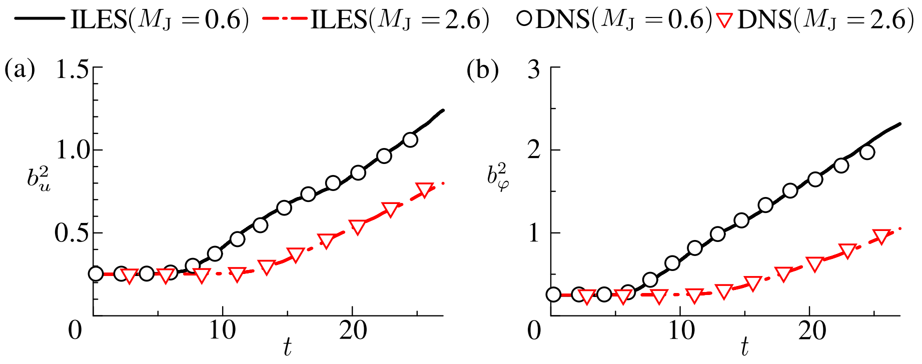

FIGURE 5 Temporal evolutions of squared jet half-width defined with lateral profiles of (a) mean streamwise velocity and (b) mean scalar. DNS results are also shown for comparison [25].

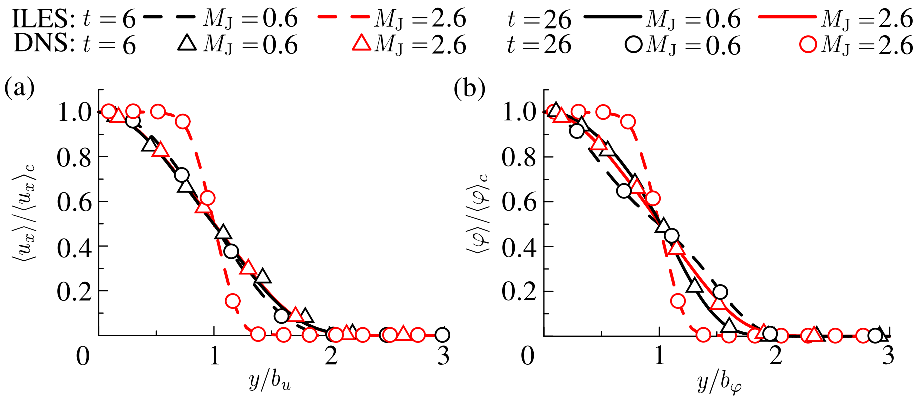

FIGURE 6 Lateral profiles of (a) mean streamwise velocity and (b) mean passive scalar normalized by their values at $y = 0$. DNS results are also shown for comparison [25].

normalized by the mean streamwise velocity $\langle u_x \rangle_c$ or the mean scalar $\langle \varphi \rangle_c$ at the center of the jet. The rms fluctuations tend to be smaller for the higher Mach number, and this Mach number dependence is predicted well by the ILES.

The passive scalar field is further examined by a probability density function (PDF) of φ at $y = 0$ and b_φ in Figure 8. The center of the jet has the PDF with a single peak while the PDF at $y = b_\varphi$ has an extremely large value at $\varphi = 0$. This is due to the outer intermittency of the jet, and the different shapes of the PDF at $y = 0$ and b_φ are well captured by the ILES. At $y = b_\varphi$, the peak at $\varphi = 0$ is smaller for $M_J = 2.6$ than for $M_J = 0.6$. This is because the engulfment of the ambient flow with $\varphi = 0$ is suppressed with increasing the Mach number as visualized in Figure 3. This Mach number dependence of the passive scalar statistics is also well captured by the ILES.

The evolution of the mean scalar in the turbulent jet is dominated by the lateral turbulent scalar flux defined as $\langle \rho u_y' \varphi' \rangle$. Figure 9 shows the lateral profiles of $\langle \rho u_y' \varphi' \rangle$ in the DNS and ILES. Because the jet development is delayed at a higher Mach number, larger positive and negative peaks of $\langle \rho u_y' \varphi' \rangle$ appear closer to the centerline at $M_J = 2.6$ compared with $M_J = 0.6$ at

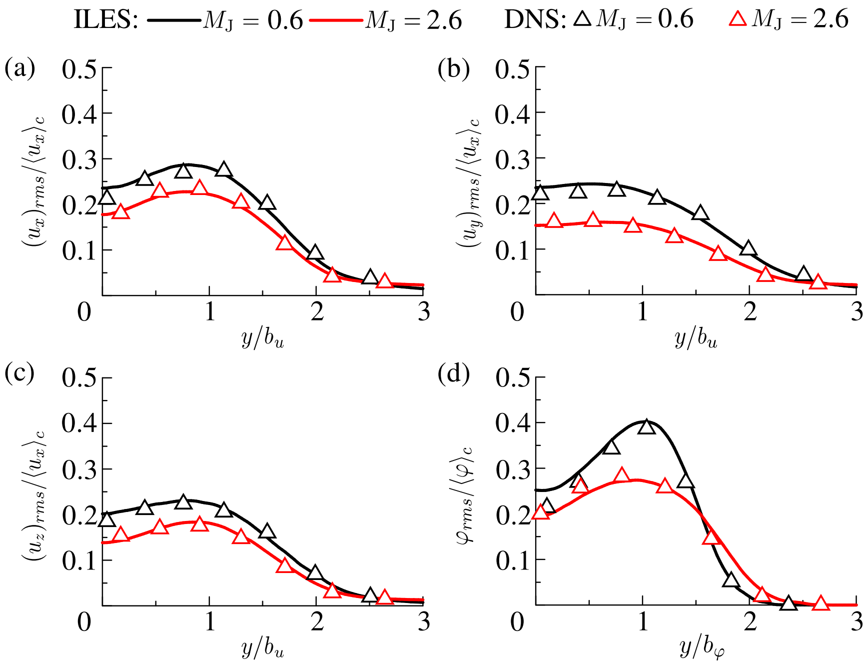

FIGURE 7 Lateral profiles of rms velocity and scalar fluctuations at $t = 26$ in ILES and DNS [25]: (a) streamwise velocity $(u_x)_{rms}/\langle u_x\rangle_c$, (b) lateral velocity $(u_y)_{rms}/\langle u_x\rangle_c$, (c) spanwise velocity $(u_z)_{rms}/\langle u_x\rangle_c$, and (d) scalar $\varphi_{rms}/\langle\varphi\rangle_c$.

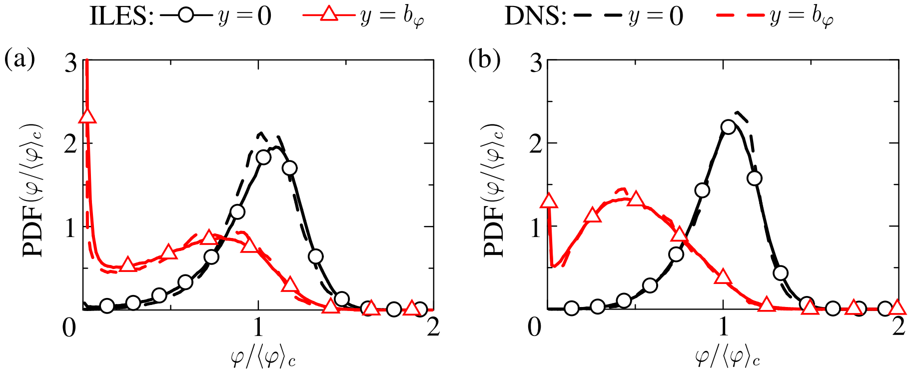

FIGURE 8 Probability density function (PDF) of passive scalar at $t = 26$ for (a) $M_J = 0.6$ and (b) 2.6.

the same time. The ILES predicts well the turbulent scalar flux at both Mach numbers, which also explains the good agreements in the mean scalar profile between the ILES and DNS.

Figure 10 compares $\langle\varphi\rangle$ and φ_{rms} in the ILES between the fine grid with $(N_x, N_y, N_z) = (480, 300, 240)$ and the coarse grid with $(N_x, N_y, N_z) = (360, 300, 180)$. These quantities hardly depend on the grid size examined here. Both mean value and rms fluctuations are governed by large-scale characteristics of the flow, and the insensitivity to the resolution indicates that large-scale fluctuations of the turbulent jet are well resolved with both grid settings.

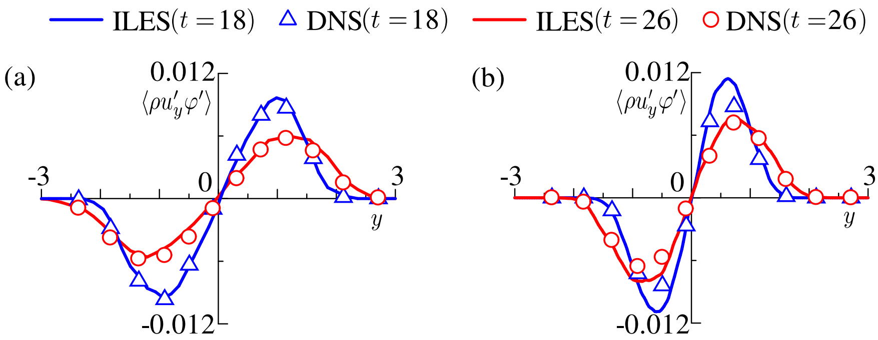

FIGURE 9 Lateral profiles of turbulent scalar flux $\langle \rho u'_y \varphi' \rangle$ at (a) M_J = 0.6 and (b) 2.6.

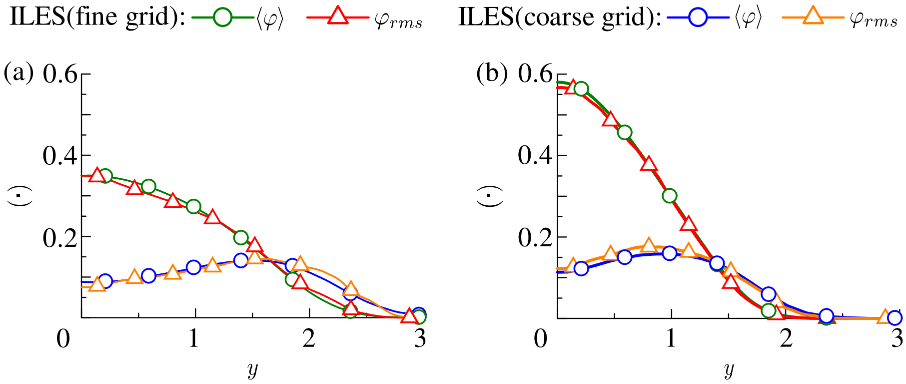

FIGURE 10 Effects of the grid size of ILES on mean scalar $\langle \varphi \rangle$ and rms scalar fluctuations φ_{rms} at t = 26 for (a) M_J = 0.6 and (b) M_J = 2.6.

4.4 | Model contribution to the dissipation of turbulent kinetic energy and scalar variance

This subsection evaluates the contribution of the filters to the dissipation of turbulent kinetic energy and scalar variance. For the definition of the turbulent kinetic energy and scalar variance in compressible flows, it is useful to define a Favre average as $[f] = \langle \rho f \rangle / \langle \rho \rangle$, while fluctuations of f from $[f]$ are denoted by $f'' = f - [f]$. The turbulent kinetic energy and scalar variance are defined as $\langle \rho u''_k u''_k \rangle = \langle \rho \rangle [u''_k u''_k]$ and $\langle \rho \varphi''^2 \rangle = \langle \rho \rangle [\varphi''^2]$, respectively. In the ILES used in this study, the selective filter and the shock-capturing filter are used as the implicit SGS model, which dissipates the turbulent kinetic energy and scalar variance. Hereafter, $\overline{f}$ denotes a variable after all filters are applied to a variable f. We introduce the filter term F expressed as

$$F(f) = \frac{1}{\Delta t} \left(\overline{f} - f \right). \tag{18}$$

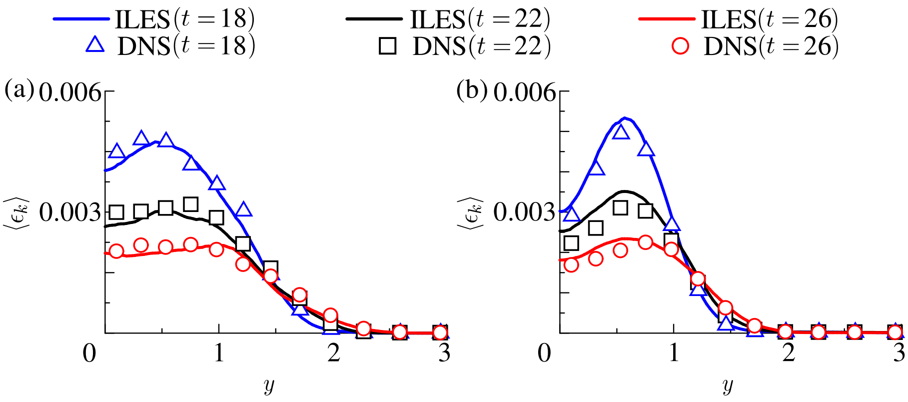

FIGURE 11 Comparisons of turbulent kinetic energy dissipation rate between ILES and DNS [25]: (a) $M_J = 0.6$; (b) $M_J = 2.6$.

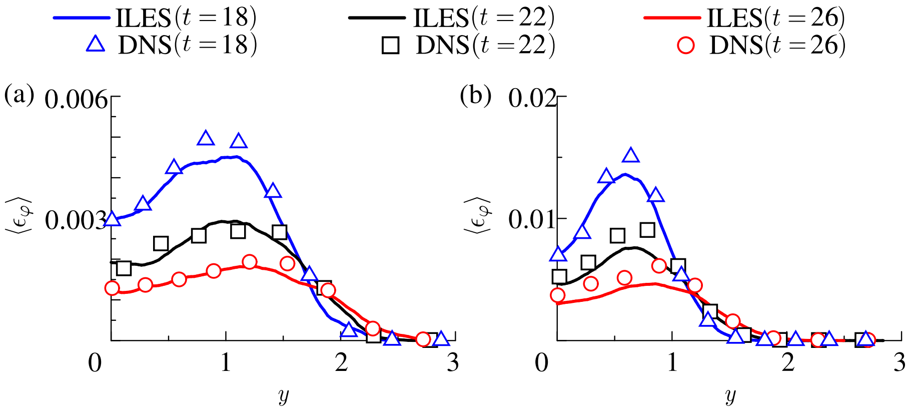

FIGURE 12 Comparisons of scalar variance dissipation rate between ILES and DNS [25]: (a) $M_J = 0.6$; (b) $M_J = 2.6$.

The governing equations for ρ and $\rho\varphi$ in the ILES can be rewritten with F as

$$\frac{\partial \rho}{\partial t} + \frac{\partial \rho u_j}{\partial x_j} = F(\rho), \tag{19}$$

$$\frac{\partial \rho\varphi}{\partial t} + \frac{\partial \rho\varphi u_j}{\partial x_j} = \rho\left(\frac{\partial \varphi}{\partial t} + u_j\frac{\partial \varphi}{\partial x_j}\right) + \varphi\left(\frac{\partial \rho}{\partial t} + \frac{\partial \rho u_j}{\partial x_j}\right) = \frac{1}{ScRe}\frac{\partial}{\partial x_j}\left(\mu\frac{\partial \varphi}{\partial x_j}\right) + F(\rho\varphi), \tag{20}$$

Here, the advection term for $\rho\varphi$ is rewritten in the non-conservative form in Eq. (20). We multiply Eq. (20) by $2\varphi''$ after Eq. (19) is substituted in Eq. (20), and take an average $\langle\ \rangle$ to obtain the following equation:

$$\underbrace{2\left\langle \rho\varphi''\frac{\partial \varphi}{\partial t}\right\rangle}_{\text{A}} + \underbrace{2\left\langle \rho\varphi'' u_j\frac{\partial \varphi}{\partial x_j}\right\rangle}_{\text{B}} = \underbrace{2\frac{1}{ScRe}\left\langle \varphi''\frac{\partial}{\partial x_j}\left(\mu\frac{\partial \varphi}{\partial x_j}\right)\right\rangle}_{\text{C}} + 2\left\langle \varphi'' F(\rho\varphi)\right\rangle - 2\left\langle \varphi''\varphi F(\rho)\right\rangle. \tag{21}$$

Terms A and B can be rewritten as

$$\mathrm{A} = 2\left\langle \rho\varphi'' \right\rangle \frac{\partial[\varphi]}{\partial t} + \left\langle \frac{\partial \rho\varphi''^2}{\partial t} \right\rangle - \left\langle \varphi''^2 \frac{\partial \rho}{\partial t} \right\rangle = \left\langle \frac{\partial \rho\varphi''^2}{\partial t} \right\rangle - \left\langle \varphi''^2 \frac{\partial \rho}{\partial t} \right\rangle, \tag{22}$$

$$\begin{aligned} \mathrm{B} &= 2\langle \rho\varphi'' \rangle [u_j] \frac{\partial[\varphi]}{\partial x_j} + 2\langle \rho\varphi'' u_j'' \rangle \frac{\partial[\varphi]}{\partial x_j} + 2\left\langle \rho\varphi'' u_j \frac{\partial \varphi''}{\partial x_j} \right\rangle \\ &= 2\langle \rho\varphi'' u_j'' \rangle \frac{\partial[\varphi]}{\partial x_j} + \frac{\partial}{\partial x_j}\left\langle \rho u_j \varphi''^2 \right\rangle - \left\langle \varphi''^2 \frac{\partial \rho u_j}{\partial x_j} \right\rangle \\ &= 2\left\langle \rho\varphi'' u_j'' \right\rangle \frac{\partial[\varphi]}{\partial x_j} + \frac{\partial \left\langle \rho\varphi''^2 \right\rangle [u_j]}{\partial x_j} + \frac{\partial}{\partial x_j}\langle \rho u_j'' \varphi''^2 \rangle - \left\langle \varphi''^2 \frac{\partial \rho u_j}{\partial x_j} \right\rangle, \end{aligned} \tag{23}$$

where $\langle \rho\varphi'' \rangle = \langle \rho\varphi \rangle - \langle \rho \rangle [\varphi] = 0$ is used. Term C is rewritten as

$$\mathrm{C} = \frac{2}{ScRe} \left\langle \frac{\partial}{\partial x_j}\left(\mu\varphi'' \frac{\partial \varphi}{\partial x_j} \right) \right\rangle - \frac{2}{ScRe} \left\langle \mu \frac{\partial \varphi}{\partial x_j} \frac{\partial \varphi''}{\partial x_j} \right\rangle. \tag{24}$$

Then, the governing equation for the scalar variance is obtained from Eqs. (21-24) as

$$\begin{aligned} \frac{\partial \left\langle \rho\varphi''^2 \right\rangle}{\partial t} + \frac{\partial \langle \rho\varphi''^2 \rangle [u_j]}{\partial x_j} &= -2\langle \rho\varphi'' u_j'' \rangle \frac{\partial[\varphi]}{\partial x_j} - \frac{\partial}{\partial x_j}\langle \rho u_j'' \varphi''^2 \rangle + \frac{2}{ScRe}\left\langle \frac{\partial}{\partial x_j}\left(\mu\varphi'' \frac{\partial \varphi}{\partial x_j} \right) \right\rangle \\ &\quad - \left\langle \frac{2}{ScRe} \mu \frac{\partial \varphi}{\partial x_j} \frac{\partial \varphi''}{\partial x_j} \right\rangle - \left\langle -\varphi''^2 F(\rho) - 2\varphi'' F(\rho\varphi) + 2\varphi''\varphi F(\rho) \right\rangle. \end{aligned} \tag{25}$$

The last two terms are the dissipation terms by the grid scales and filters. Therefore, the instantaneous dissipation rates of $\langle \rho\varphi''^2 \rangle = \langle \rho \rangle [\varphi''^2]$ by the grid scales ($\epsilon_\varphi^{(GS)}$) and by the filters ($\epsilon_\varphi^{(SGS)}$) can be written as

$$\epsilon_\varphi^{(GS)} = \frac{2\mu}{ScRe}\left(\frac{\partial \varphi}{\partial x_j} \frac{\partial \varphi''}{\partial x_j} \right), \tag{26}$$

$$\epsilon_\varphi^{(SGS)} = -\varphi''^2 F(\rho) - 2\varphi'' F(\rho\varphi) + 2\varphi''\varphi F(\rho). \tag{27}$$

For the turbulent kinetic energy, the dissipation rates by the grid scales and by the filters are denoted by $\epsilon_k^{(GS)}$ and $\epsilon_k^{(SGS)}$, respectively. Averages of these terms appear in the governing equation for $\langle \rho u_k'' u_k'' \rangle$, which can be derived from the equations for ρ and ρu_i with the filtering operator F. The derivation of $\epsilon_k^{(GS)}$ and $\epsilon_k^{(SGS)}$ is similar to that of $\epsilon_\varphi^{(GS)}$ and $\epsilon_\varphi^{(SGS)}$, and was presented in detail in [40], where $\epsilon_k^{(GS)}$ and $\epsilon_k^{(SGS)}$ are shown to be written as

$$\epsilon_k^{(GS)} = \frac{1}{Re}\tau_{ij}\frac{\partial u_i''}{\partial x_j}, \tag{28}$$

$$\epsilon_k^{(SGS)} = -u_i'' F(\rho u_i) + u_i'' u_i F(\rho) - \frac{1}{2}u_i''^2 F(\rho). \tag{29}$$

In the DNS used for comparison with the ILES, the turbulent kinetic energy and scalar variance are dissipated solely at grid scales. Therefore, their dissipation rates are defined as $\epsilon_k = \epsilon_k^{(GS)}$ and $\epsilon_\varphi = \epsilon_\varphi^{(GS)}$, whose expressions are identical to Eqs. (26) and (28).

Figures 11 and 12 compare the averaged dissipation rates of the turbulent kinetic energy and scalar variance between the DNS and ILES. Here, the overall dissipation rates in the ILES are evaluated as $\epsilon_k = \epsilon_k^{(GS)} + \epsilon_k^{(SGS)}$ and $\epsilon_\varphi = \epsilon_\varphi^{(GS)} + \epsilon_\varphi^{(SGS)}$. For both

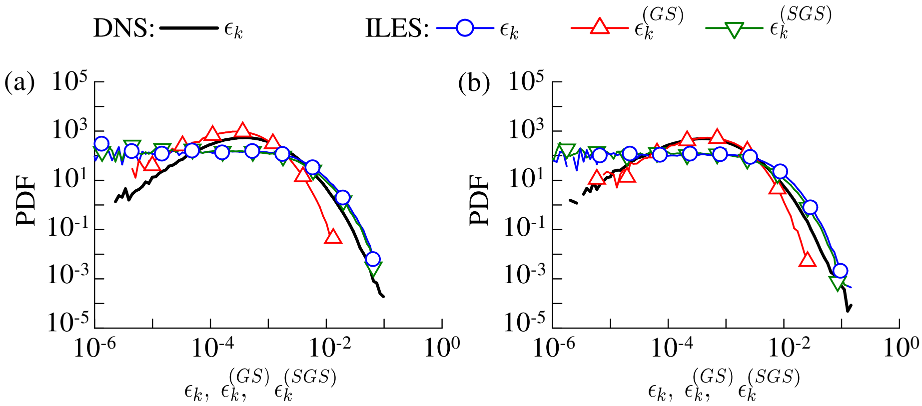

FIGURE 13 Probability density functions of $\epsilon_k = \epsilon_k^{(GS)} + \epsilon_k^{(SGS)}$, $\epsilon_k^{(GS)}$, and $\epsilon_k^{(SGS)}$ at $t = 22$ in ILES: (a) $M_J = 0.6$; (b) $M_J = 2.6$. The PDF of ϵ_k in DNS [25] is also shown for comparison.

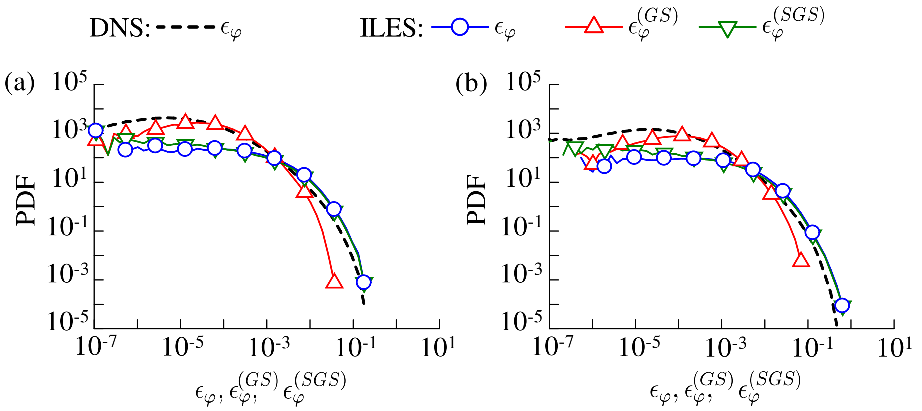

FIGURE 14 Probability density functions of $\epsilon_\varphi = \epsilon_\varphi^{(GS)} + \epsilon_\varphi^{(SGS)}$, $\epsilon_\varphi^{(GS)}$, and $\epsilon_\varphi^{(SGS)}$ at $t = 22$ in ILES: (a) $M_J = 0.6$; (b) $M_J = 2.6$. The PDF of ϵ_φ in DNS [25] is also shown for comparison.

high and low Mach numbers, the dissipation rates in the ILES are consistent with the DNS results, and the filters used as the implicit SGS model account for the accurate amount of the dissipation that occurs in the SGS. Figure 13 shows the PDF of $\epsilon_k^{(GS)}$, $\epsilon_k^{(SGS)}$, and ϵ_k at both Mach numbers. The PDF of the dissipation rate of scalar variance is shown in Figure 14. These figures also show the PDF of ϵ_k and ϵ_φ in the DNS. The lines of the PDF are not shown when the probability is zero. The dissipation rates due to the filters can be as large as the instantaneous dissipation rates in the DNS. The probability of large dissipation rates is higher for $\epsilon_k^{(SGS)}$ and $\epsilon_\varphi^{(SGS)}$ than for the grid-scale contributions, and the intense dissipation of the turbulent kinetic energy and scalar variance is caused by the filters. In turbulence, regions with large dissipation rates of velocity and scalar fluctuations are associated with small-scale fluctuations, which appear intermittently in space. Therefore, the dissipation in these regions cannot be expressed on the grid used in the ILES, and is treated with the filters. On the other hand, the PDF of $\epsilon_k^{(GS)}$ and $\epsilon_\varphi^{(GS)}$ has a peak for moderately large dissipation rates, for which the probability is low for the filter contributions. Therefore, moderately

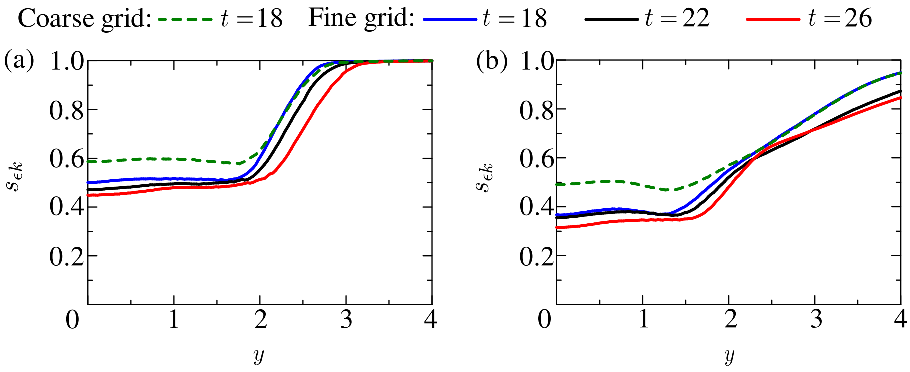

FIGURE 15 Relative contributions of the implicit SGS model to turbulent kinetic energy dissipation rate: (a) $M_J = 0.6$; (b) $M_J = 2.6$.

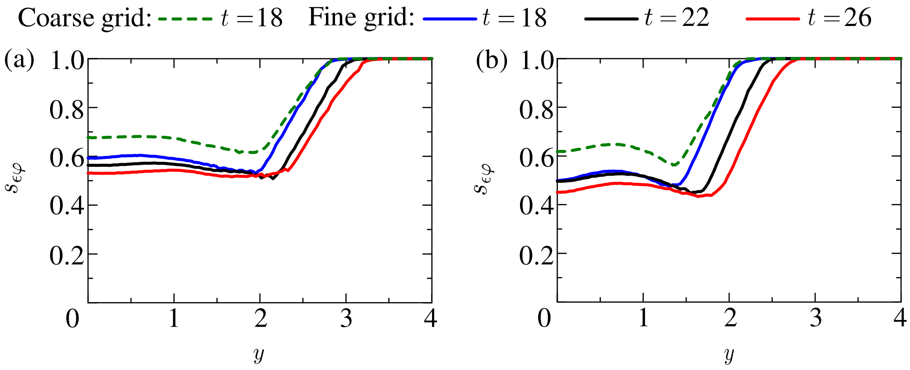

FIGURE 16 Relative contributions of the SGS model to scalar variance dissipation rate: (a) $M_J = 0.6$; (b) $M_J = 2.6$.

large dissipation rates are associated with large-scale velocity and scalar gradients, which can be resolved on the grid used in the ILES.

The relative contribution of the implicit SGS model to the overall dissipation rate can be evaluated as below [41]:

$$s_{\epsilon k} = \frac{\left\langle \epsilon_k^{(SGS)} \right\rangle}{\left\langle \epsilon_k^{(GS)} \right\rangle + \left\langle \epsilon_k^{(SGS)} \right\rangle}, \quad s_{\epsilon\varphi} = \frac{\left\langle \epsilon_\varphi^{(SGS)} \right\rangle}{\left\langle \epsilon_\varphi^{(GS)} \right\rangle + \left\langle \epsilon_\varphi^{(SGS)} \right\rangle}. \tag{30}$$

Figures 15 and 16 show the lateral profiles of $s_{\epsilon k}$ and $s_{\epsilon\varphi}$, respectively. The results with the coarse grid at $t = 18$ are also shown in these figures. $s_{\epsilon k}$ and $s_{\epsilon\varphi}$ for the fine grid are close to 0.4-0.6 in the jet, and almost half of the dissipation is caused by the filters. $s_{\epsilon k}$ and $s_{\epsilon\varphi}$ are larger for the coarse grid than the fine grid, and the SGS (filter) contribution to the dissipation becomes relatively smaller when the ILES has a better spatial resolution. Both $s_{\epsilon k}$ and $s_{\epsilon\varphi}$ increase toward 1 with y, and the dissipation outside the jet is mostly caused by the filters. However, $s_{\epsilon k}$ for $M_J = 2.6$ is still smaller than 1 even outside the jet with large y, and grid-scale fluctuations also contribute to the turbulent kinetic energy dissipation rate. Figure 17 shows the two-dimensional profiles of $\epsilon_k^{(SGS)}$, $\epsilon_k^{(GS)}$, and dilatation $\Theta = \partial u_j/\partial x_j$. The supersonic jet with $M_J = 2.6$ generates strong pressure waves propagating

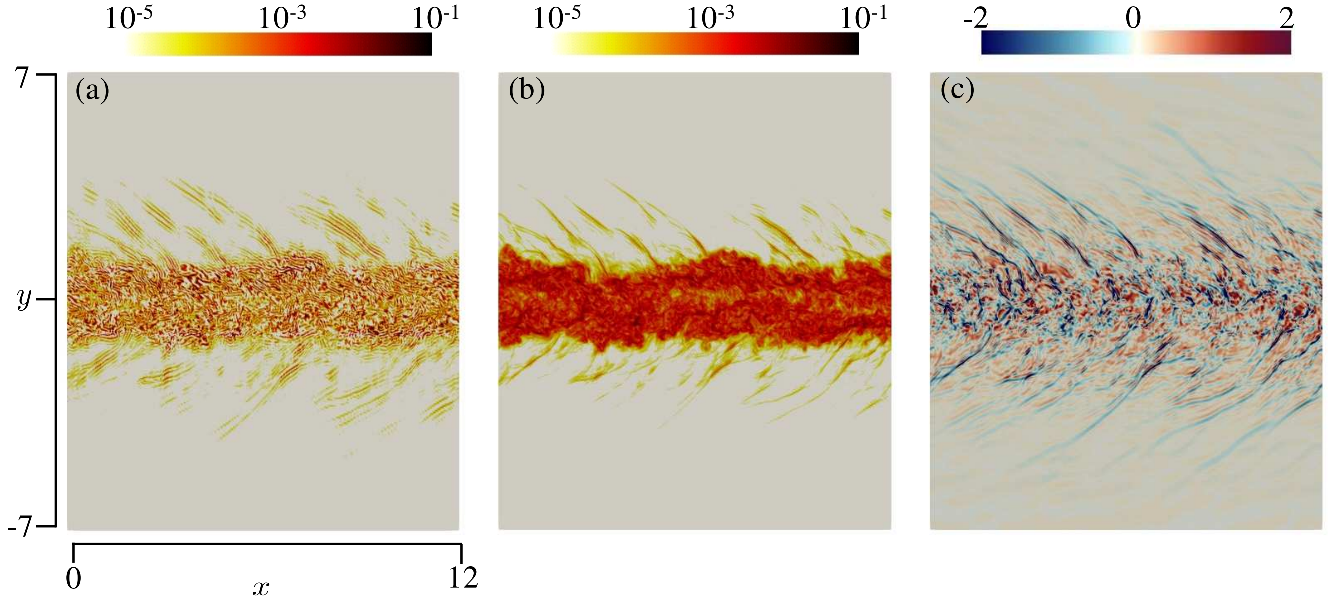

FIGURE 17 Two-dimensional profiles of (a) $\epsilon_k^{(SGS)}$, (b) $\epsilon_k^{(GS)}$, and (c) $\Theta = \partial u_j/\partial x_j$ at $M_J = 2.6$ ($t = 18$).

outside the jet as visualized in Figure 17(c). Profiles of $\epsilon_k^{(SGS)}$, $\epsilon_k^{(GS)}$, and Θ outside the jet are strongly correlated with each other. These waves induce velocity fluctuations, which contribute to the turbulent kinetic energy dissipation by $\epsilon_k^{(SGS)}$ and $\epsilon_k^{(GS)}$. Visualization of $\epsilon_k^{(SGS)}$ exhibits oscillations near the strong pressure waves since the unphysical oscillations in the velocity field can be caused by velocity jumps across the waves. Figure 17 indicates that $\epsilon_k^{(SGS)}$ dumps the unphysical fluctuations caused by the strong waves. The grid-scale contribution $\epsilon_k^{(GS)}$ is not negligible outside the jet, and the velocity fluctuations induced by the waves are partially dissipated by $\epsilon_k^{(GS)}$ as confirmed by $s_{\epsilon k} < 1$ in Figure 15(b). On the other hand, $s_{\epsilon\varphi}$ in Figure 16 increases to 1 with y for both Mach numbers because the pressure waves do not produce scalar fluctuations outside the jets. Therefore, contrary to the profiles of $s_{\epsilon k}$, the location where $s_{\epsilon\varphi}$ reaches 1 is closer to the center of the jet at $M_J = 0.6$ than at $M_J = 2.6$ because of the delay of the jet development caused by compressibility effects.

5 | CONCLUSIONS

The ILES is tested for the passive scalar transfer in the subsonic and supersonic planar jets. The present ILES relies on fully-explicit numerical schemes for the spatial and temporal discretization and the implicit SGS model that is comprised of the low-pass filter and the shock-capturing filter. The ILES is evaluated by comparisons with the DNS databases. Various statistics confirm that the ILES used in this study predicts well the evolution of the turbulent planar jet with passive scalar transfer for both subsonic and supersonic cases. The ILES also predicts well the turbulent scalar flux, which dominates the mean scalar evolution in the turbulent jet. It is well known that a higher jet Mach number results in the delay of the jet development, which affects temporal evolutions of the statistics. The Mach number dependence of the turbulent jet is well captured by the ILES. The dissipation rates of turbulent kinetic energy and scalar variance are contributed by both grid scale and subgrid scale. The SGS dissipation rates of the turbulent kinetic energy and scalar variance in the ILES are directly evaluated with the filtering operator. The dissipation rate in the ILES, calculated as the sum of the grid-scale and filter (SGS) contributions, is consistent with the dissipation rate obtained in the DNS for both high and low Mach numbers. Under the present numerical conditions, the SGS dissipation rate accounts for 40-60% of the total dissipation rate in the fully-developed turbulent jet. The dissipation rates by the filters become as large as the instantaneous dissipation rates observed in the DNS, and the regions with intense dissipations in the turbulent jet are treated with the filters. The supersonic jet generates strong pressure waves, which induce the velocity fluctuations outside the jet. Therefore, the turbulent kinetic energy dissipation rate for the grid scale does not reach 0 even outside the supersonic jet. The unphysical oscillations caused by the shock-like waves are dumped by the SGS dissipation rate.

ACKNOWLEDGMENTS

The numerical simulations presented in this manuscript were carried out on the high-performance computing system (NEC SX-ACE) in the Japan Agency for Marine-Earth Science and Technology. This work was partially supported by “Collaborative Research Project on Computer Science with High-Performance Computing in Nagoya University” and by JSPS KAKENHI Grant Number 18K13682 and 18H01367.

DATA AVAILABILITY

The data that support the findings of this study are available from the corresponding author upon reasonable request.

References

[1] Laget O, Kleemann A, Jay S, Reveille B, Henriot S. Gasoline engine development using CFD. *SAE Technical Paper.* 2005: No. 2005-01-3814.

[2] Takahashi H, Ikegami S, Oso H, Masuya G, Hirota M. Quantitative imaging of injectant mole fraction and density in a supersonic mixing. *AIAA J.* 2008; 46(11): 2935–2943.

[3] Smagorinsky J. General circulation experiments with the primitive equations: I. The basic experiment. *Mon Weather Rev.* 1963; 91(3): 99–164.

[4] DeBonis JR, Scott JN. Large-eddy simulation of a turbulent compressible round jet. *AIAA J.* 2002; 40(7): 1346–1354.

[5] Wegner B, Huai Y, Sadiki A. Comparative study of turbulent mixing in jet in cross-flow configurations using LES. *Int J Heat Fluid Flow.* 2004; 25(5): 767–775.

[6] Bogey C, Bailly C. Decrease of the effective Reynolds number with eddy-viscosity subgrid modeling. *AIAA J.* 2005; 43(2): 437–439.

[7] Bogey C, Bailly C. Effects of inflow conditions and forcing on a Mach 0.9 jet and its radiated noise. *AIAA J.* 2005; 43(5): 1000–1007.

[8] Leonard A. Energy cascade in large-eddy simulations of turbulent fluid flows, In: Advances in geophysics. 1975; 18: 237–248.

[9] Boris JP. On large eddy simulation using subgrid turbulence models Comment 1, In: Whither turbulence? Turbulence at the crossroads. 1990: 344–353.

[10] Visbal MR, Rizzetta DP. Large-eddy simulation on curvilinear grids using compact differencing and filtering schemes. *J Fluids Eng.* 2002; 124(4): 836–847.

[11] Mathew J, Lechner R, Foysi H, Sesterhenn J, Friedrich R. An explicit filtering method for large eddy simulation of compressible flows. *Phys Fluids.* 2003; 15(8): 2279–2289.

[12] Hahn M, Drikakis D. Large eddy simulation of compressible turbulence using high-resolution methods. *Int J Numer Meth Fluids.* 2005; 47(8-9): 971–977.

[13] Uranga A, Persson PO, Drela M, Peraire J. Implicit large eddy simulation of transition to turbulence at low Reynolds numbers using a discontinuous Galerkin method. *Int J Numer Meth Engng.* 2011; 87(1-5): 232–261.

[14] De Wiart CC, Hillewaert K, Bricteux L, Winckelmans G. Implicit LES of free and wall-bounded turbulent flows based on the discontinuous Galerkin/symmetric interior penalty method. *Int J Numer Meth Fluids.* 2015; 78(6): 335–354.

[15] Vermeire BC, Nadarajah S, Tucker PG. Implicit large eddy simulation using the high-order correction procedure via reconstruction scheme. *Int J Numer Meth Fluids.* 2016; 82(5): 231–260.

[16] Watanabe T, Sakai Y, Nagata K, Ito Y. Large eddy simulation study of turbulent kinetic energy and scalar variance budgets and turbulent/non-turbulent interface in planar jets. *Fluid Dyn Res.* 2016; 48(2): 021407.

[17] Hickel S, Adams NA, Mansour NN. Implicit subgrid-scale modeling for large-eddy simulation of passive-scalar mixing. *Phys Fluids.* 2007; 19(9): 095102.

[18] Watanabe T, Sakai Y, Nagata K, Ito Y, Hayase T. Implicit large eddy simulation of a scalar mixing layer in fractal grid turbulence. *Phys. Scr.* 2016; 91(7): 074007.

[19] Watanabe T, Nagata K. Mixing model with multi-particle interactions for Lagrangian simulations of turbulent mixing. *Phys Fluids.* 2016; 28(8): 085103.

[20] Remmler S, Hickel S. Direct and large eddy simulation of stratified turbulence. *Int J Heat Fluid Flow.* 2012; 35: 13–24.

[21] Colucci PJ, Jaberi FA, Givi P, Pope SB. Filtered density function for large eddy simulation of turbulent reacting flows. *Phys Fluids.* 1998; 10(2): 499–515.

[22] Le Ribault C, Simoëns S, Vinkovic I. Hybrid large eddy simulation/Lagrangian stochastic model for turbulent passive and reactive scalar dispersion in a plane jet. *Chem Eng Commun.* 2012; 199(4): 435–460.

[23] Watanabe T, Sakai Y, Nagata K, Ito Y, Hayase T. LES–Lagrangian particle method for turbulent reactive flows based on the approximate deconvolution model and mixing model. *J Comput Phys.* 2015; 294: 127–148.

[24] Cleary MJ, Klimenko AY. A generalised multiple mapping conditioning approach for turbulent combustion. *Flow Turbul Combust.* 2009; 82(4): 477.

[25] Tai Y, Watanabe T, Nagata K. Modeling of molecular diffusion and thermal conduction with multi-particle interaction in compressible turbulence. *Phys Fluids.* 2018; 30(3): 035108.

[26] Zhang X, Watanabe T, Nagata K. Turbulent/nonturbulent interfaces in high-resolution direct numerical simulation of temporally evolving compressible turbulent boundary layers. *Phys Rev Fluids.* 2018; 3(9): 094605.

[27] Nagata R, Watanabe T, Nagata K. Turbulent/non-turbulent interfaces in temporally evolving compressible planar jets. *Phys Fluids.* 2018; 30(10): 105109.

[28] Lodato G, Domingo P, Vervisch L. Three-dimensional boundary conditions for direct and large-eddy simulation of compressible viscous flows. *J Comput Phys.* 2008; 227(10): 5105–5143.

[29] Wang Z, Lv Y, He P, Zhou J, Cen K. Fully explicit implementation of direct numerical simulation for a transient near-field methane/air diffusion jet flame. *Comput Fluids.* 2010; 39(8): 1381–1389.

[30] Bogey C, Bailly C. A family of low dispersive and low dissipative explicit schemes for flow and noise computations. *J Comput Phys.* 2004; 194(1): 194–214.

[31] Kennedy CA, Carpenter MH. Several new numerical methods for compressible shear-layer simulations. *Appl Numer Math.* 1994; 14(4): 397–433.

[32] Bogey C, De Cacqueray N, Bailly C. A shock-capturing methodology based on adaptative spatial filtering for high-order non-linear computations. *J Comput Phys.* 2009; 228(5): 1447–1465.

[33] Kempf A, Klein M, Janicka J. Efficient generation of initial-and inflow-conditions for transient turbulent flows in arbitrary geometries. *Flow Turbul Combust.* 2005; 74(1): 67–84.

[34] Bogey C, Bailly C. Large eddy simulations of transitional round jets: influence of the Reynolds number on flow development and energy dissipation. *Phys Fluids.* 2006; 18(6): 065101.

[35] Wang Z, He P, Lv Y, Zhou J, Fan J, Cen K. Direct numerical simulation of subsonic round turbulent jet. *Flow Turbul Combust.* 2010; 84(4): 669–686.

[36] Clemens NT, Mungal MG. Large-scale structure and entrainment in the supersonic mixing layer. *J Fluid Mech.* 1995; 284: 171–216.

[37] Freund JB, Moin P, Lele SK. Compressibility effects in a turbulent annular mixing layer. Part 2. Mixing of a passive scalar. *J Fluid Mech.* 2000; 421: 269–292.

[38] Westerweel J, Fukushima C, Pedersen JM, Hunt JCR. Momentum and scalar transport at the turbulent/non-turbulent interface of a jet. *J Fluid Mech.* 2009; 631: 199–230.

[39] Chevray R, Tutu NK. Intermittency and preferential transport of heat in a round jet. *J. Fluid Mech.* 1978; 88(1): 133–160.

[40] Bogey C, Bailly C. Turbulence and energy budget in a self-preserving round jet: direct evaluation using large eddy simulation. *J Fluid Mech.* 2009; 627: 129–160.

[41] Geurts BJ, Fröhlich J. A framework for predicting accuracy limitations in large-eddy simulation. *Phys Fluids.* 2002; 14(6): L41–L44.